Mon. Not. R. Astron. Soc. **000**, 1–9 (2021) Printed 27 January 2021 (MN LATEX style file v2.2)

Off-axis jet scenario for early afterglow emission of low-luminosity gamma-ray burst GRB 190829A

Yuri Sato[1⋆], Kaori Obayashi[1]†, Ryo Yamazaki[1,2]‡, Kohta Murase[3,4,5,6]§ and Yutaka Ohira[7]¶

[1] *Department of Physics and Mathematics, Aoyama Gakuin University, 5-10-1 Fuchinobe, Sagamihara 252-5258, Japan*
[2] *Institute of Laser Engineering, Osaka University, 2-6 Yamadaoka, Suita, Osaka 565-0871, Japan*
[3] *Department of Physics, Pennsylvania State University, University Park, Pennsylvania 16802, USA*
[4] *Department of Astronomy & Astrophysics, Pennsylvania State University, University Park, Pennsylvania 16802, USA*
[5] *Center for Multimessenger Astrophysics, Pennsylvania State University, University Park, Pennsylvania 16802, USA*
[6] *Center for Gravitational Physics, Yukawa Institute for Theoretical Physics, Kyoto University, Kyoto, Kyoto 606-8502, Japan*
[7] *Department of Earth and Planetary Science, The University of Tokyo, 7-3-1 Hongo, Bunkyo-ku, Tokyo 113-0033, Japan*

today

ABSTRACT

Recently, ground-based Imaging Atmospheric Cherenkov Telescopes have reported the detection of very-high-energy (VHE) gamma rays from some gamma-ray bursts (GRBs). One of them, GRB 190829A, was triggered by the *Swift* satellite, and about 2×10^4 s after the burst onset the VHE gamma-ray emission was detected by H.E.S.S. with $\sim 5\sigma$ significance. This event had unusual features of having much smaller isotropic equivalent gamma-ray energy than typical long GRBs and achromatic peaks in X-ray and optical afterglow at about 1.4×10^3 s. Here we propose an off-axis jet scenario that explains these observational results. In this model, the relativistic beaming effect is responsible for the apparently small isotropic gamma-ray energy and spectral peak energy. Using a jetted afterglow model, we find that the narrow jet, which has the initial Lorentz factor of 350 and the initial jet opening half-angle of 0.015 rad, viewed off-axis can describe the observed achromatic behavior in the X-ray and optical afterglow. Another wide, baryon-loaded jet is necessary for the later-epoch X-ray and radio emissions. According to our model, the VHE gamma rays observed by H.E.S.S. at 2×10^4 s may come from the narrow jet through the synchrotron self-Compton process.

Key words: gamma-ray bursts: individual: GRB 190829A — radiation mechanisms: non-thermal

1 INTRODUCTION

Recently, very-high-energy (VHE) gamma-rays from some gamma-ray bursts (GRBs) were detected by ground-based Imaging Atmospheric Cherenkov Telescopes, such as the Major Atmospheric Gamma Imaging Cherenkov (MAGIC) telescopes, and the High Energy Stereoscopic System (H.E.S.S.). A prototypical example so far is GRB 190114C, which was simultaneously detected with MAGIC and *Fermi* Large Area Telescope (MAGIC Collaboration, et al. 2019a,b; Ajello et al. 2020). The observed spectrum in the VHE gamma-ray band is well explained by the synchrotron self-Compton (SSC) model (MAGIC Collaboration, et al. 2019b; Derishev & Piran 2019; Fraija et al. 2019a,b,c; Wang, et al. 2019; Asano et al. 2020; Huang et al. 2020b). H.E.S.S. detected VHE gamma-rays from GRB 180720B about 10 hours after the burst onset at 5.3 σ significance level, and the energy flux was $\nu F_\nu \approx 5\times10^{-11}$erg s^{-1}cm^{-2} in the VHE band (Abdalla, et al. 2019). GRB 190829A was also detected by H.E.S.S. about 2×10^4 s after the burst trigger (de Naurois et al. 2019). Its significance is ~ 5 σ. Moreover, a possible detection of VHE gamma-ray emission from a short GRB 160821B has been claimed by MAGIC (MAGIC Collaboration, et al. 2020; Zhang et al. 2020b). It is expected that in the near future, the Cherenkov Telescope Array (CTA; Actis et al. 2011) will increase the number of GRBs with VHE gamma-rays (Kakuwa, et al. 2012; Gilmore, et al. 2013; Inoue, et al. 2013).

⋆ E-mail: yuris@phys.aoyama.ac.jp (YS)
† E-mail: o-kaori@phys.aoyama.ac.jp (KO)
‡ E-mail: ryo@phys.aoyama.ac.jp (RY)
§ E-mail: murase@psu.edu (KM)
¶ E-mail: y.ohira@eps.s.u-tokyo.ac.jp (YO)

Compared with GRB 190114C and 180720B, GRB 190829A has some peculiar observational properties. The prompt gamma-ray emission (from $\sim$ 10 keV to MeV band) consists of two temporally separated components (Chand et al. 2020). The burst started with less energetic emission (hereafter Episode 1 following Chand et al. 2020) with an isotropic equivalent gamma-ray energy of $E_{\rm iso,\gamma} = 3.2 \times 10^{49}$ erg and a peak energy (that is, the photon energy at which the νF_ν-spectrum takes a maximum) $E_p = 120$ keV. After quiescent time interval lasting about 40 s, the second brighter emission (Episode 2) with $E_{\rm iso,\gamma} = 1.9 \times 10^{50}$ erg and $E_p = 11$ keV, appeared. The observed values of $E_{\rm iso,\gamma}$ and E_p of Episode 2 are consistent with Amati relation (Amati et al. 2002; Sakamoto et al. 2008), while those of Episode 1 are in the region of low-luminosity GRBs. Both Episode 1 and 2 have smaller $E_{\rm iso,\gamma}$ and E_p than typical long GRBs, including the other VHE gamma-ray events, GRB 190114C and 180720B (e.g., Huang et al. 2020a). Indeed, GRB 190829A occurred so nearby with a redshift of $z = 0.0785$ that such weak prompt emissions could be observed.

Well-sampled afterglow light curves of GRB 190829A were obtained in X-ray, optical/infrared (IR) (Chand et al. 2020), and radio bands (Rhodes et al. 2020). It is remarkable that early X-ray and optical/IR afterglow emission showed a rising part and simultaneously peaked at about 1.4×10^3 s. Such an "achromatic" behavior is difficult to be explained in standard afterglow model, in which the synchrotron emission has the maximum when the typical frequency ν_m crosses the observation bands (Sari, Piran & Narayan 1998). In contrast, the other VHE events, GRB 190114C and 180720B, showed monotonically decaying X-ray afterglow emission (Yamazaki et al. 2020; Fraija et al. 2019b). Possible interpretations of the achromatic bump are the X-ray flare with optical counterpart (Chand et al. 2020; Zhang et al. 2020a; Zhao et al. 2020b) and the afterglow onset of baryon loaded outflow with bulk Lorentz factor of about 30 (Fraija et al. 2020).

In this paper, we propose an off-axis jet scenario to explain the observed properties of GRB 190829A. If the jet is viewed off-axis, the relativistic beaming effect causes apparently dim and soft prompt emission (Ioka & Nakamura 2001, 2018; Yamazaki, Ioka, & Nakamura 2002, 2003, 2004a,b; Yamazaki, Yonetoku, & Nakamura 2003; Salafia et al. 2015, 2016). Some low-luminosity GRBs may be explained by this context (e.g., Yamazaki, Yonetoku, & Nakamura 2003; Ramirez-Ruiz et al. 2005). This model may also explain observed achromatic behavior of early X-ray and optical/IR afterglow with a maximum at 1.4×10^3 s. For the off-axis afterglow (e.g., Granot et al. 2002), the bulk Lorentz factor of the jet is initially so high that the afterglow emission is very dim because of the relativistic beaming effect. As the jet decelerates, the beaming effect becomes weak, resulting in the emergence of a rising part in afterglow light curves. After the peak of the emission, the jet has smaller Lorentz factors so that the light curve only weakly depends on the viewing angle. This paper is organized as follows. In § 2, we construct our afterglow model following Huang et al. (2000). For simplicity, the jet is assumed to be uniform, and structured jets (e.g., Rossi, Lazzati, & Rees 2002; Zhang & Mészáros 2002; Zhang et al. 2004) are not considered. In § 3, we show that our model explains the observed afterglow in the X-ray, optical, and radio bands. In order to explain the observed data, we need two jets with narrow and wide opening angles (see Fig. 1). The former is viewed off-axis, while the other is not. Such a two-compornet jet model (e.g., Peng, Königl, & Granot 2005; Racusin et al. 2008) might be supported by the fact that the prompt emission has two independent components. In § 4, VHE gamma-ray flux at 2×10^4 s is estimated. In § 5, using a simple model, we discuss the on-axis prompt emission properties of the narrow jet. Section 6 is devoted to a discussion. In this paper, cosmological parameters $H_0 = 71$ km s^{-1} Mpc^{-1}, $\Omega_M = 0.27$, and $\Omega_\Lambda = 0.23$ (Spergel et al. 2003) are adopted following Chand et al. (2020), whose values of $E_{\rm iso,\gamma}$ and E_p are directly used in this paper. Then, the luminosity distance to GRB 198029A is 0.35 Gpc.

2 MODEL DESCRIPTION OF JETTED AFTERGLOW

In this section, following Huang et al. (2000), we describe a model of jet dynamics and associated synchrotron emission. Let t_b and r be the time and radial coordinates, respectively, in the rest frame of the central engine located at the origin, $r = 0$. In this frame, the polar angle θ is set such that the central axis of the jet corresponds to $\theta = 0$. We assume a uniform jet with a thin shell emitting region at radius R. The jet velocity is

$$\beta c = \frac{dR}{dt_b} \ , \tag{1}$$

where c is the speed of light, and the bulk Lorentz factor is $\Gamma = 1/\sqrt{1-\beta^2}$. In the central engine frame, the jet is ejected from the central engine at $t_b = 0$. Initially, the jet has the opening half-angle θ_0, isotropic-equivalent kinetic energy $E_{\rm iso,K}$ and the initial bulk Lorentz factor Γ_0. Ambient interstellar matter (ISM) is assumed to be uniform with the number density n_0. The jet decelerates via interactions with ISM and forms a thin shell. The decrease of Γ is given by

$$\frac{d\Gamma}{dm} = -\frac{\Gamma^2 - 1}{M_{ej} + \epsilon m + 2(1-\epsilon)\Gamma m} \ , \tag{2}$$

where $M_{\rm ej} = E_{\rm iso,K}/\Gamma_0 c^2$ and ϵ_γ are ejecta mass and the radiative efficiency, respectively, and m is the swept-up mass (see, e.g., Huang et al. 2000). For our parameters adopted in § 3, the value of ϵ_γ is too small to affect our results. It is geometrically related to the shell radius R and the jet opening half-angle θ_j as

$$\frac{dm}{dR} = 2\pi R^2 (1 - \cos\theta_j) n_0 m_p \ , \tag{3}$$

where m_p is the mass of the proton. We assume that the jet spreads laterally at the sound speed c_s measured in the shell comoving frame (see Pe'er 2012; Nava et al. 2013, for more detailed treatments on the dynamical evolution of calculations of the gas temperature), and set the increase of the jet opening half-angle as

$$\frac{d\theta_j}{dt_b} = \frac{c_s}{\Gamma R} \ . \tag{4}$$

Solving Eqs. (1)–(4), we get the jet dynamics, that is, Γ and θ_j as a function of time. Following the standard convention,

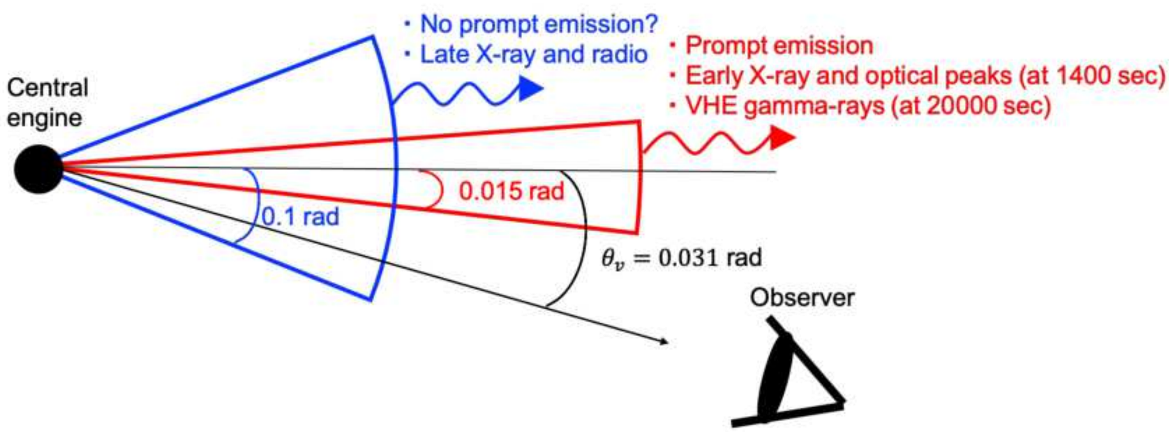

Figure 1. Schematic view of our two-component jet model for GRB 190829A. The red and blue cones represent narrow and wide jets, respectively. Initial shapes of the jets are depicted with their initial opening half-angles. The black arrow shows the observer's line of sight. As the jets expand, they spread sideways, and at $\sim 2\times10^4$ s when H.E.S.S. detected VHE gamma-rays, the observer's line of sight is inside the cone of the narrow jet.

their time evolution is shown with the on-axis observer ($\theta = 0$) time t which is related to t_b by

$$\frac{dt}{dt_b} = 1 - \beta \quad . \tag{5}$$

In calculating synchrotron radiation, we assume that microphysics parameters ϵ_e and ϵ_B, the energy fractions of internal energy going into radiating electrons and magnetic field, are constant. The electron energy distribution in the emitting thin shell has a power-law form with index p. In the slow cooling regime, the electron spectrum has a break at the electron cooling Lorentz factor γ_c, where we take into account the SSC cooling in the Thomson limit as well as synchrotron energy losses (Dermer, Chiang, & Mitman 2000; Sari & Esin 2001; Zhang & Mészáros 2001). Then, it has a form $N(\gamma_e) \propto {\gamma_e}^{-p}$ when $\gamma_m < \gamma_e < \gamma_c$ and $N(\gamma_e) \propto {\gamma_e}^{-p-1}$ when $\gamma_c < \gamma_e$.

We assume that the observer's line of sight is $\theta = \theta_v$. The flux density F_ν of the afterglow emission that arrives at the observer time T is obtained by integrating the emissivity over the equal arrival time surface determined by

$$\int \frac{1-\beta\cos\Theta}{\beta c} dR = \frac{T}{1+z} \quad , \tag{6}$$

where Θ is the angle between the radial direction at each emitter position and the line of sight (e.g., Granot, Piran, & Sari 1999). In summary, parameters of the present model are isotropic-equivalent kinetic energy $E_{\rm iso,K}$, initial Lorentz factor Γ_0, initial jet opening half-angle θ_0, ISM density n_0, microphysical parameters ϵ_e and ϵ_B, electron power-law index p, and the viewing angle θ_v.

3 NUMERICAL RESULTS FOR AFTERGLOW EMISSION

In this section, we show our numerical results of synchrotron afterglow emission in the X-ray (10^{18} Hz), optical (V-band), and radio (1.3 and 15.5 GHz) bands, and compare them with observation data of GRB 190829A. The X-ray data are extracted from the *Swift* team website[1] (Evans et al. 2007, 2009) which provides us with the integrated energy flux in the 0.3–10 keV band and the photon indices at some epoch. The index was around 2.2 at any time. On the other hand, we numerically calculate the energy flux density $F_{\nu=10^{18}\,\rm Hz}$. In order to compare theoretical and observational results, we convert the observed integrated energy flux to the flux density at 10^{18} Hz assuming that the photon index is 2.2 at any time. The optical V-band data (before the absorption correction) are obtained from Chand et al. (2020). In our numerical calculation, we take the V-band extinction $A_{\rm V} = 1.5$ mag (Chand et al. 2020). The radio data are taken from Rhodes et al. (2020).

[1] https://www.swift.ac.uk/xrt_curves/00922968/

3.1 Off-axis afterglow emission from a narrow jet

First, we consider a single jet viewed off-axis in order to discuss the observed X-ray and optical bumps around $T \sim 1.4 \times 10^2$ s. We adopt $\theta_v = 0.031$ rad, $\theta_0 = 0.015$ rad, $E_{\rm iso,K} = 4.0 \times 10^{53}$ erg, $\Gamma_0 = 350$, $n_0 = 0.01$ cm^{-3}, $\epsilon_e = 0.2$, $\epsilon_B = 5.0 \times 10^{-5}$ and $p = 2.44$. The initial opening half-angle is small, so that we refer to "narrow jet" in the following. Solid lines in the left panel of Fig. 2 show our results. Our off-axis afterglow model well explains the observational results of early X-ray and optical afterglow from about 8×10^2 to 2×10^4 s. An achromatic behavior in the X-ray and optical bands is evident. The off-axis afterglow starts with a rising part because of the relativistic beaming effect (Granot et al. 2002). As the jet decelerates, the observed flux increases. When the jet Lorentz factor becomes $\Gamma \sim (\theta_v - \theta_0)^{-1} = 65$, the afterglow light curve takes a maximum. After that, the observed flux is almost the same as that in the case of on-axis viewing ($\theta_v = 0$: dashed lines in the left panel of Fig. 2). If we assume the adiabatic evolution ($\Gamma \propto t^{-3/8}$), the observer time of the flux maximum is analytically given by

$$T_{pk} \sim (1+z) \left(\frac{3E_{\rm iso,K}}{4\pi n_0 m_p c^5} \right)^{\frac{1}{3}} (\theta_v - \theta_0)^{\frac{8}{3}} \quad . \tag{7}$$

For our model parameters, we get $T_{pk} \sim 2 \times 10^3$ s, which is consistent with our numerical results within a factor of two. As shown in Fig. 3 (thick-red-solid and dot-dashed lines), the scaling $\Gamma \propto t^{-3/8}$ is roughly a good approximation until $t \sim 10^4$ s, since the jet spreading effect is not significant (see the thick red line in Fig. 4). This fact validates the estimate of T_{pk} by Eq. (7). For comparison, the dashed lines in the left panel of Fig. 2 show the light curves in the on-axis viewing case ($\theta_v = 0$), in which the X-ray flux peaks much earlier than the optical one (Sari, Piran & Narayan 1998).

After several tens of thousand seconds after the burst onset, our numerically calculated X-ray light curve deviates from the observed data (see the left panel of Fig. 2). Before that epoch, the sideway expansion of the jet is not significant (thick-red-solid line in Fig. 4). As the jet decelerates, the jet becomes trans-relativistic ($\Gamma \lesssim 10$) around $t \sim 10^5$ s, and then θ_j begins rapid increase (Zhang & MacFadyen 2009)[2]. Then, our numerical result shows that the jet dynamics asymptotically reaches the scaling $\Gamma \propto t^{-1/2}$ (black-dotted line in Fig. 3), at which the observed X-ray flux follows the scaling $F_\nu \propto t^{-p} = t^{-2.44}$ (Sari, Piran, & Halpern 1999). This slope is much steeper than observed. Hence, it is difficult for the narrow jet to explain the observed late X-ray afterglow as well as radio emission at late times. In the next section § 3.2, we add another component to enhance the late X-ray and radio fluxes.

[2] In the past literature, it used to be assumed that a relativistic jet rapidly decelerates and its opening angle increases exponentially just after the jet break time which is given by $t_{\rm jet} \sim (3E_{\rm iso,K}/4\pi n_0 m_p c^5)^{1/3} \theta_0^{8/3}$ (Sari, Piran, & Halpern 1999), and for our model parameters, we get $t_{\rm jet} \sim 2 \times 10^3$ s. However, as shown by relativistic hydrodynamics simulation by Zhang & MacFadyen (2009), the lateral expansion is not significant until the trans-relativistic phase.

3.2 Two-component jet model

Second, we consider a two-component jet model, in which another "wide jet" is introduced in addition to the narrow jet considered in § 3.1. The observed flux is simply the superposition of each jet emission components. The parameters of the narrow jet are the same as those given in § 3.1. For the wide jet, we adopt $\theta_0 = 0.1$ rad, $E_{\rm iso,K} = 2.0 \times 10^{53}$ erg, $\Gamma_0 = 20$, $\epsilon_e = 0.4$, $\epsilon_B = 1.0 \times 10^{-5}$, and $p = 2.2$. The values of θ_v and n_0 are common for both jets. It is assumed that the central axes of the two jets are identical ($\theta = 0$: see Fig. 1).

One can find in the right panel of Figure 2 that early achromatic peaks in the X-ray and optical bands are explained by the off-axis narrow jet emission (dashed lines in the right panel), and that the late X-ray and radio afterglow is interpreted with the wide jet emission (dotted lines). As shown in the thin-blue-solid line in Fig. 3, the wide jet does not decelerate until $t \sim 5 \times 10^4$ s, since it is heavy with a low bulk Lorentz factor, $\Gamma_0 = 20$. Our numerical result (dotted lines in the right panel of Fig. 2) shows that X-ray and optical flux becomes maximum around this epoch. The wide jet becomes trans-relativistic ($\Gamma \lesssim 10$) at $t \sim 10^5$ s and finally enters to the Newtonian phase at $t \gtrsim 10^6$ s. We find that for 10^5 s $\lesssim t \lesssim 10^7$ s, the absorption frequency ν_a, typical frequency ν_m and cooling frequency ν_c obeys the relation $\nu_a < \nu_m < \nu_c$. The value of ν_c is located between the optical and the X-ray bands, and ν_m is lower than the optical band. Then, the X-ray and optical fluxes follow the scalings $F_\nu \propto t^{-(3p-4)/2} = t^{-1.3}$ and $F_\nu \propto t^{-3(5p-7)/10} = t^{-1.2}$, respectively (e.g., Gao et al. 2013), which is consistent with the observation. The typical frequency ν_m decreases with time, and at $t \sim 4 \times 10^5$ s, it crosses 15.5 GHz, at which the 15.5 GHz light curve has a peak. After that, the flux follows the scaling $F_\nu \propto t^{-3(5p-7)/10} = t^{-1.2}$ (e.g., Gao et al. 2013). Subsequently, ν_m intersects 1.3 GHz at $t \sim 1 \times 10^6$ s, and the 1.3 GHz flux takes maximum, after which the flux decays in the same manner. These radio behavior is roughly consistent with the observation. Note that if the initial bulk Lorentz factor of the wide jet Γ_0 is larger than 20, our numerical X-ray light curve is brighter than the observed data in earlier epoch.

4 VHE GAMMA-RAY EMISSION AT 2×10^4 SECONDS

In this section, we estimate the VHE gamma-ray flux at 2×10^4 s along with our two-component jet model considered in § 3. For simplicity, the SSC flux at $h\nu = 0.1$ TeV is calculated in the Thomson limit (Sari & Esin 2001). The flux attenuation by extragalactic background light at 0.1 TeV is negligible because the source is nearby (Zhang et al. 2020a).

For both narrow and wide jets, we get the bulk Lorentz factor Γ of the jets and the synchrotron spectrum F_ν at 2×10^4 s as seed photons for SSC emission. First, we consider the narrow jet, which has the bulk Lorentz factor $\Gamma \simeq 20$, the post-shock magnetic field $B \simeq 5.4 \times 10^{-3}$ G, the minimum electron Lorentz factor $\gamma_m \simeq 2.2 \times 10^3$, the electron cooling Lorentz factor $\gamma_c \simeq 1.3 \times 10^6$ $[14/(1+Y)]$, the typical frequency $\nu_m \simeq 7.7 \times 10^{12}$ Hz, the cooling frequency $\nu_c \simeq 6.9 \times 10^{17}$ $[14/(1+Y)]^2$ Hz and the peak flux

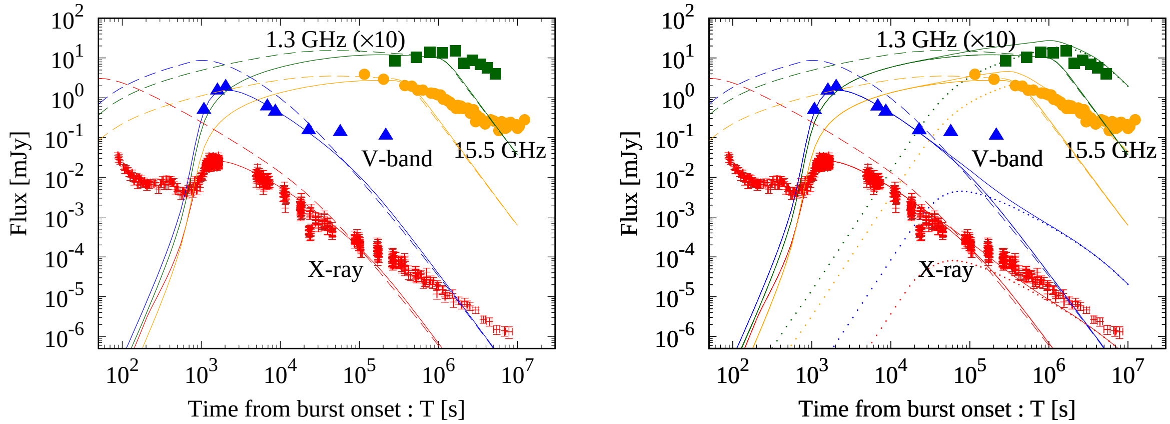

Figure 2. Afterglow light curves in the X-ray (10^{18} Hz: red), optical (V-band: blue) and radio bands (1.3 GHz: orange, 15.5 GHz: green), which is compared with the observed data of GRB 190829A (X-ray: red points, V-band: blue triangles, 1.3 GHz: orange filled-circles, 15.5 GHz: green squares). In the left panel, solid and dashed lines show the emission from the narrow jet ($\theta_0 = 0.015$ rad, $E_{\rm iso,K} = 4.0 \times 10^{53}$ erg, $\Gamma_0 = 350$, $n_0 = 0.01$ cm^{-3}, $\epsilon_e = 0.2$, $\epsilon_B = 5.0 \times 10^{-5}$ and $p = 2.44$), which is viewed off-axis ($\theta_v = 0.031$ rad) and on-axis ($\theta_v = 0$), respectively. In the right panel, we show the results of our two-component jet model — solid lines are the sum of the narrow (dashed lines) and wide (dotted lines) jets. The latter has parameters, $\theta_v = 0.031$ rad, $\theta_0 = 0.1$ rad, $E_{\rm iso,K} = 2.0 \times 10^{53}$ erg, $\Gamma_0 = 20$, $n_0 = 0.01$ cm^{-3}, $\epsilon_e = 0.4$, $\epsilon_B = 1.0 \times 10^{-5}$ and $p = 2.2$.

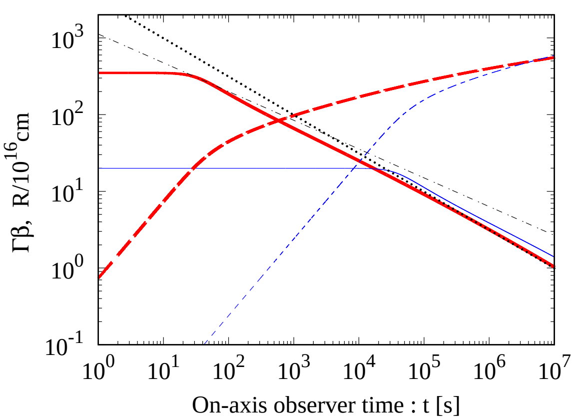

Figure 3. The four-velocity $\Gamma\beta$ (solid lines) and radius R (dashed lines) of narrow (thick-red lines) and wide (thin-blue lines) jets as a function of the on-axis observer time t. The black dot-dashed and dotted lines represent analytical scalings $\Gamma\beta \propto t^{-3/8}$ (adiabatic evolution without sideway expansion) and $\Gamma\beta \propto t^{-1/2}$ (adiabatic evolution with sideway expansion), respectively.

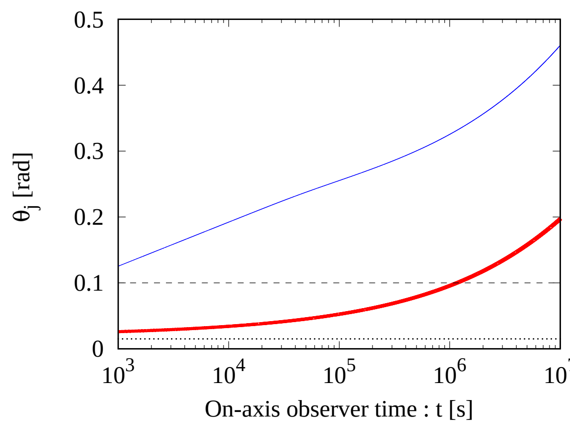

Figure 4. Jet opening half-angle θ_j as a function of the on-axis observer time t. Thick-red-solid and thin-blue-solid curves are for narrow and wide jets, respectively. Two horizontal dotted and dashed lines are the initial values (0.015 rad and 0.1 rad for the narrow and wide jets, respectively).

$F_{\rm max} = F_{\nu=\nu_m} \simeq 1.4 \times 10$ mJy. Then, the break frequencies for the SSC emission (Sari & Esin 2001) are given by $\nu_m^{\rm IC} \approx 2\gamma_m^2 \nu_m \simeq 7.5 \times 10^{19}$Hz and $\nu_c^{\rm IC} \approx 2\gamma_c^2 \nu_c \simeq 2.3 \times 10^{30}\ [14/(1+Y)]^4$ Hz. One can find that the observation photon energy $h\nu = 0.1$ TeV satisfies $\sqrt{\nu_m^{\rm IC}\nu_c^{\rm IC}} < \nu < \nu_c^{\rm IC}$, so that the SSC flux is calculated by

$$F_\nu^{\rm SSC} \approx 0.5 R \sigma_T n_0 F_{\rm max} \frac{(p-1)}{(p+1)} \left(\frac{\nu}{\nu_m^{\rm IC}}\right)^{(1-p)/2} \times \left[2\frac{(2p+3)}{(p+2)} - \frac{2}{(p+1)(p+2)} + \ln\left(\frac{\nu_c^{\rm IC}}{\nu}\right)\right] \quad (8)$$

where σ_T is the Thomson cross section. Hence, the SSC energy flux from the narrow jet is estimated as $\nu F_\nu^{\rm SSC} \sim 1.2 \times 10^{-11}$ erg s^{-1}cm^{-2}. Since the jet energy is large, we have a lot of seed photons from its own synchrotron radiation to get detectable SSC emission. In reality, the Klein-Nishina effect becomes important below $\nu_c^{\rm IC}$. The Y parameter at γ_c is significantly reduced due to the Klein-Nishina effect, so the VHE gamma-ray flux is expected to have a peak around TeV energies below $\nu_c^{\rm IC}$ in the Thomson limit. Correspondingly, the value of ν_c would be underestimated.

Similarly, we calculate the SSC flux from the wide jet. At 2×10^4 s, we have $\Gamma \simeq 20$, $B \simeq 2.4 \times 10^{-3}$ G, $\gamma_m \simeq 2.4 \times 10^3$, $\gamma_c \simeq 2.4 \times 10^6\ [10/(1+Y)]$, $\nu_m \simeq 1.0 \times 10^{12}$ Hz, $\nu_c \simeq 1.0 \times 10^{18}\ [10/(1+Y)]^2$ Hz, and $F_{\rm max} \simeq 0.1$ mJy, so that we obtain $\nu_m^{\rm IC} \simeq 1.1 \times 10^{19}$ Hz and $\nu_c^{\rm IC} \simeq 1.1 \times 10^{31}\ [10/(1+Y)]^4$ Hz, resulting in $\nu F_\nu^{\rm SSC} \sim 2 \times 10^{-14}$

erg s^{-1}cm^{-2} at $h\nu = 0.1$ TeV. The narrow jet is predominant at VHE gamma-ray band at about 2×10^4 s. Just around this epoch, the wide jet is in the transition from the free expansion to the adiabatic deceleration phase. Indeed, as shown by the dotted lines in the right panel of Fig. 2, we see a rising part in X-ray and optical bands. After 2×10^4 s, the SSC flux from the wide jet might increase just for a while. However, it would soon start to decrease and keep subdominant.

We discuss the time dependence of the VHE gamma-ray flux between $\sim 10^4$ and $\sim 10^5$ s in the Thomson limit. In this epoch, the observed flux for $\theta_v = 0.031$ hardly changes from that for $\theta_v = 0$ (for narrow jets, see the left panel of Fig. 2), so that the standard analytical calculation for on-axis observer is a good approximation for the present case. We find that for both jets, the break frequencies of the narrow and wide jets at $h\nu = 0.1$ TeV satisfies $\nu_m^{\rm IC} < \nu < \nu_c^{\rm IC}$ at any time, so that the SSC flux is given by $F_\nu^{\rm SSC} \propto R\sigma_T n_0 F_{\rm max}(\nu/\nu_m^{\rm IC})^{(1-p)/2}$. For the narrow jet, the Lorentz factor is approximated to follow the scaling $\Gamma \propto t^{-1/2}$ (see the thick-red-dashed line in Fig. 3). Then for synchrotron component, we have $\gamma_m \propto t^{-1/2}$, $\nu_m \propto t^{-2}$ and $F_{\rm max} \propto t^{-1}$ (Sari, Piran, & Halpern 1999), so that $\nu_m^{\rm IC} \propto t^{-3}$ and $F_\nu^{\rm SSC} \propto t^{-(3p-1)/2} = t^{-3.16}$. On the other hand, as discussed in the previous paragraph, the VHE flux from the wide jet has brighten, following the analytical scaling $F_\nu^{\rm SSC} \propto t^4$ until $t \sim 5 \times 10^4$ s at the transition from the free expansion to the adiabatic deceleration phase. After this time, the flux decays. For the jet dynamics $\Gamma \propto t^{-3/8}$ ($\propto t^{-1/2}$), we get the VHE flux $F_\nu^{\rm SSC} \propto t^{-(9p-11)/8} = t^{-1.1}$ ($\propto t^{-(3p-1)/2} = t^{-2.8}$). Such a time evolution could have been observed with good statistics by more sensitive detectors like CTA.

5 PROMPT EMISSION PROPERTIES OF NARROW JET

The prompt emission of GRB 190829A had smaller values of the peak energy $E_{\rm p}$ and the isotropic-equivalent gamma-ray energy $E_{{\rm iso},\gamma}$ than typical long GRBs. In this section, we discuss whether $E_{\rm p}$ and $E_{{\rm iso},\gamma}$ from our narrow jet were typical or not if it would have been viewed on-axis ($\theta_v \approx 0$). We consider a very simple analytical model (e.g., Ioka & Nakamura 2001; Yamazaki, Ioka, & Nakamura 2002, 2003) assuming an instantaneous emission of an infinitesimally thin shell moving with the Lorentz factor $\Gamma_0 = 1/\sqrt{1-\beta_0^2}$. The jet is uniform, whose intrinsic emission properties do not vary with angle, and has a sharp edge at the opening half-angle θ_0. Then, the viewing-angle dependence of the peak energy, $E_p(\theta_v)$, and isotropic-equivalent gamma-ray energy, $E_{{\rm iso},\gamma}(\theta_v)$, can be analytically calculated (Donaghy 2006; Graziani, Lamb, & Donaghy 2006), and we obtain

$$\begin{aligned} R_1 &= \frac{E_{\rm p}(\theta_v)}{E_{\rm p}(0)} \\ &= \frac{2(1-\beta_0)(1-\beta_0\cos\theta_0)}{2-\beta_0(1+\cos\theta_0)} \\ &\quad \times \frac{f(\beta_0-\cos\theta_v) - f(\beta_0\cos\theta_0-\cos\theta_v)}{g(\beta_0-\cos\theta_v) - g(\beta_0\cos\theta_0-\cos\theta_v)} \ , \end{aligned} \tag{9}$$

$$\begin{aligned} R_2 &= \frac{E_{{\rm iso},\gamma}(\theta_v)}{E_{{\rm iso},\gamma}(0)} \\ &= \frac{(1-\beta_0)^2(1-\beta_0\cos\theta_0)^2}{\beta_0(1-\cos\theta_0)[2-\beta_0(1+\cos\theta_0)]} \\ &\quad \times [f(\beta_0-\cos\theta_v) - f(\beta_0\cos\theta_0-\cos\theta_v)] \ , \end{aligned} \tag{10}$$

where, functions f and g are given by

$$f(z) = \frac{\Gamma_0^2(2\Gamma_0^2-1)z^3 + (3\Gamma_0^2\sin^2\theta_v - 1)z + 2\cos\theta_v\sin^2\theta_v}{|z^2 + \Gamma_0^{-2}\sin^2\theta_v|^{\frac{3}{2}}} \ , \tag{11}$$

and

$$g(z) = \frac{2\Gamma_0^2 z + 2\cos\theta_v}{|z^2 + \Gamma_0^{-2}\sin^2\theta_v|^{\frac{1}{2}}} \ , \tag{12}$$

respectively (see also Urata et al. 2015). For parameters of our narrow jet given in § 3.1 ($\Gamma_0 = 350$, $\theta_0 = 0.015$ rad and $\theta_v = 0.031$ rad), we get $R_1 = 3.2 \times 10^{-2}$ and $R_2 = 1.2 \times 10^{-4}$.

If the narrow jet emitted Episode 1 of observed prompt emission (see § 1), that is, $E_p(\theta_v = 0.031) = 120$ keV and $E_{{\rm iso},\gamma}(\theta_v = 0.031) = 3.2 \times 10^{49}$ erg (Chand et al. 2020), then on-axis quantities are obtained as $E_p(0) = E_p(\theta_v)/R_1 = 3.7$ MeV and $E_{{\rm iso},\gamma}(0) = E_{{\rm iso},\gamma}(\theta_v)/R_2 = 2.7 \times 10^{53}$ erg. These values are within the range for bursts detected so far (e.g., Zhao et al. 2020a). The isotropic equivalent kinetic energy of the narrow jet just after the prompt emission is $E_{\rm iso,K} = 4.0 \times 10^{53}$ erg (see § 3.1), so that the efficiency of the prompt emission is calculated as $\eta_\gamma = E_{{\rm iso},\gamma}(0)/(E_{{\rm iso},\gamma}(0) + E_{\rm iso,K}) \approx 0.4$. On the other hand, if the narrow jet is responsible for Episode 2 (that is, $E_p(\theta_v = 0.031) = 11$ keV and $E_{{\rm iso},\gamma}(\theta_v = 0.031) = 1.9 \times 10^{50}$ erg), we obtain $E_p(0) = 340$ keV and $E_{{\rm iso},\gamma}(0) = 1.6 \times 10^{54}$ erg, which are again similar to typical long GRBs. In this case, the efficiency is $\eta_\gamma \approx 0.8$.

The observed prompt emission had two episodes (see § 1), while in § 3 we showed two jets are required to explain the observed afterglow. At present, it is unknown if the two episodes corresponds to the two jets. If the narrow jet causes Episode 1, then the estimated prompt emission efficiency η_γ is almost typical, however on-axis $E_{\rm p}(0)$ is located at the highest end of the distribution for long GRBs. On the other hand, if the narrow jet produced Episode 2, then on-axis $E_{\rm p}(0)$ is smaller though η_γ is somewhat higher (but it is still comparable, and one can say that the value is reasonable considering very simple approximation of our prompt emission model). Episode 1 and 2 may be emitted from narrow and wide jets, respectively. Note that if the wide jet emits Episode 2, its efficiency is small, $\eta_\gamma \approx 5 \times 10^{-3}$, so that it might be natural that the narrow jet causes both Episode 1 and 2.

In this section, we simply assumed that the prompt emission was caused by a top-hat shaped jet, and obtained the ratios, $R_1 = E_p(\theta_v)/E_p(0) \sim 10^{-2}$ and $R_2 = E_{{\rm iso},\gamma}(\theta_v)/E_{{\rm iso},\gamma}(0) \sim 10^{-4}$, for our narrow jet. For off-axis jet emission, these values depend on the profile of angular distribution of the bulk Lorentz factor and intrinsic emissivity near the periphery of the jet. If the jet is structured like a Gaussian or power-law profile, then R_1 and R_2 may be larger in the off-axis case (e.g., Salafia et al. 2015), so that on-axis $E_p(0)$ and $E_{{\rm iso},\gamma}(0)$ may be smaller than the present estimates.

6 DISCUSSION

We have investigated an off-axis jet scenario in which we have invoked a two-component jet model to explain the observational results of GRB 190829A. According to our model, the early X-ray and optical afterglow was off-axis emission from the narrow jet, which may also be responsible for VHE gamma-rays detected at $\sim 2 \times 10^4$ s, and the late X-ray and radio afterglow came from the wide jet (Figure 1). Since the narrow jet was viewed off-axis, the prompt emission was dim and soft due to the relativistic beaming effect. On the other hand, the wide jet had the isotropic-equivalent kinetic energy $E_{\rm iso,K} \sim 10^{53}$ erg which was much larger than the observed isotropic equivalent gamma-ray energy $E_{\rm iso,\gamma} \sim 10^{49-50}$ erg. If the wide jet has a typical value of the efficiency of the prompt emission, our result would become inconsistent with the observational result because it is seen on-axis. Since the initial bulk Lorentz factor of the wide jet is $\Gamma_0 = 20$, the jet is likely to be dirty (i.e., highly loaded by baryons) and it may have a large optical depth. It may be as small as $\eta_\gamma = E_{\rm iso,\gamma}/(E_{\rm iso,\gamma} + E_{\rm iso,K}) \lesssim 10^{-3}$ unlike typical bright GRBs with high Lorentz factors.

There are still some observed components that are brighter than the prediction of our jet model. They may be other components. For example, very early ($T \lesssim 7 \times 10^2$ s) X-ray emission should be the contribution from late prompt emission like flares. The observed optical flux later than $\sim 5 \times 10^5$ s is a supernova component (Hu et al. 2020). At the late epoch ($T \sim 10^7$ s), the 15.5 GHz radio flux also exceeds our numerical result, which could be other components such as counter-jet emission.

As seen in the right panel of Fig. 2, our theoretical radio fluxes in both 1.3 and 15.5 GHz sometimes overshot the observed ones. However, the excess is only within a factor of two, and this difference may come from the uncertainty of our simple model. More realistic modeling may solve this problem. For example, structured jets such as Gaussian jets instead of uniform jets would decrease the radio fluxes keeping the X-ray and optical brightness unchanged (e.g., Cunningham et al. 2020).

We have also estimated the VHE gamma-ray flux at 2×10^4 s and have found that the narrow jet dominates the observed gamma-ray emission. Since the synchrotron radiation is bright enough due to the large jet energy, the observed VHE gamma-ray flux, $\nu F_\nu \sim 10^{-11}$ erg s^{-1}cm^{-2}, is able to be expected by SSC mechanism. In this paper, we independently calculate two emission components from two jets. External inverse Compton with seed photons coming from the companion jet might be effective (e.g., Zhang et al. 2020a). Such an interaction between two jets remains to be future work.

Late-time ($T \sim 10^{6-7}$ s) X-ray synchrotron emission from the wide jet is about a factor of two smaller than observed data (see the red solid line in the right panel of Fig. 2). In calculating the synchrotron radiation, we have assumed the Thomson limit to derive ν_c for simplicity. If we consider the Klein-Nishina effect (Nakar, Ando, & Sari 2009; Murase et al. 2010; Wang et al. 2010; Murase et al. 2011; Jacovich, Beniamini, & van der Horst 2020; Zhang et al. 2020a), the Compton Y parameter becomes smaller, so that ν_c becomes larger. Then, the X-ray flux increases if ν_c is around the X-ray band. As a limiting test case, we have calculated the X-ray synchrotron emission setting $Y = 0$ all the time. In this case, the X-ray flux actually becomes larger but by less than ten times. It is expected that inclusion of the Klein-Nishina effect causes the increase of the hard X-ray flux. Other possibilities to have a larger X-ray flux in the late epoch include delayed energy injection (e.g., Zhang et al. 2006) and/or a low-energy part of SSC or external inverse-Compton emission (e.g., Fan et al. 2008; Zhang & Mészáros 2001; Zhang et al. 2020a).

The initial Lorentz factor of our narrow jet is $\Gamma_0 = 350$, which may be similar to or slightly smaller than those of long GRBs with VHE gamma-ray detection. For GRBs 190114C and 180720B, the afterglow onset peak time may imply the initial Lorentz factor of ≈ 500 and ≈ 450, respectively (Huang et al. 2020a). Furthermore, for both the narrow and wide jets, microphysics parameter ϵ_B is on the order of 10^{-5}, which is also similar to the other two long VHE events (Ajello et al. 2020; Fraija et al. 2019a,b,c; Wang, et al. 2019; Jordana-Mitjans et al. 2020). At present, although the number of VHE events is small, these values are common for events with detectable VHE gamma-rays. If there is no magnetic field amplification, $\epsilon_{\rm B}$ is about $10^{-7}(n_0/0.01{\rm cm}^{-3})^{-1}(B_{\rm ISM}/3\mu{\rm G})^2$, where $B_{\rm ISM}$ is the magnetic field strength for the ambient medium. Therefore, the magnetic field in the emission region of those GRB afterglows is expected to be amplified. Although the mechanism has not been understood yet (e.g., Tomita, Ohira, & Yamazaki 2019), more detailed observations of VHE gamma-rays would provide us a new hint of the magnetic field amplification mechanism (e.g., Lemoine 2015).

The initial opening half-angle of the narrow jet is $\theta_0 = 0.015$ rad. This is near the lower limit of previously measured values for long GRBs, however, it is still larger than the smallest one (Zhao et al. 2020a). In our model, the narrow jet is seen off-axis, resulting in dim prompt emission. Nevertheless, this event was observed since it occurred nearby. Hence, similar but distant ($z \gg 0.1$) events must be viewed on-axis to be detected. However, a small solid angle of the narrow jet decreases the detection rate, which may explain the small number of VHE gamma-ray events that have been detected so far.

Compared with other long GRBs with radio detection, GRB 190829A showed a lower radio afterglow luminosity (Rhodes et al. 2020), which allows us to adopt a low ambient density of $n_0 = 0.01$ cm^{-3}. However, there may be two classes in long GRBs, radio-loud and radio-quiet events (Zhang et al. 2020c). Although radio-loud GRBs have slightly larger isotropic-equivalent energies $E_{\rm iso,\gamma}$ of the prompt gamma-ray emission, the $E_{\rm iso,\gamma}$ distributions for the two classes look similar (see Fig. 11 of Zhang et al. 2020c). It might be possible that long GRBs arise in the rarefied medium. Such an environment appears when the wind of a progenitor star is strong, or the bursts occur in the superbubble made by OB association.

ACKNOWLEDGMENTS

We thank Katsuaki Asano, Kunihito Ioka, Kazumi Kashiyama, Takanori Sakamoto, Motoko Serino, Shuta J. Tanaka, and Kenji Toma for valuable comments.

This research was partially supported by JSPS KAKENHI Grant Nos. 18H01232 (RY), 20H01901 (KM), 20H05852 (KM) and JP19H01893 (YO). R.Y. deeply appreciates Aoyama Gakuin University Research Institute for helping our research by the fund. The work of K.M. is supported by NSF Grant No. AST-1908689. Y.O. is supported by Leading Initiative for Excellent Young Researchers, MEXT, Japan.

REFERENCES

Abdalla H., et al., 2019, Nature, 575, 464

Actis M., et al., 2011, ExA, 32, 193

Ajello M., et al., 2020, ApJ, 890, 9

Amati L., et al., 2002, A&A, 390, 81

Asano K., et al., 2020, arXiv:2007.06307

Chand V., et al., 2020, ApJ, 898, 42

Cunningham V., Cenko S. B., Ryan G., Vogel S. N., Corsi A., Cucchiara A., Fruchter A. S., et al., 2020, ApJ, 904, 166

Derishev E., Piran T., 2019, ApJL, 880, L27

Dermer C. D., Chiang J., Mitman K. E., 2000, ApJ, 537, 785

de Naurois M., (H. E. S. S. Collaboration), 2019, Astron. Telegram, 13052

Donaghy T. Q., 2006, ApJ, 645, 436.

Evans P. A., et al., 2007, A&A, 469, 379.

Evans P. A., et al., 2009, MNRAS, 397, 1177.

Fan Y.-Z., Piran T., Narayan R., Wei D.-M., 2008, MNRAS, 384, 1483

Fraija N., Barniol Duran R., Dichiara S., Beniamini P., 2019a, ApJ, 883, 162

Fraija N., et al., 2019b, ApJ, 885, 29

Fraija N., Dichiara S., Pedreira A. C. C. do E. S., Galvan-Gamez A., Becerra R. L., Barniol Duran R., Zhang B. B., 2019c, ApJL, 879, L26

Fraija N., Veres P., Beniamini P., Galvan-Gamez A., Metzger B. D., Barniol Duran R., Becerra R. L., 2020, arXiv, arXiv:2003.11252

Gao H., Lei W.-H., Zou Y.-C., Wu X.-F., Zhang B., 2013, NewAR, 57, 141

Gilmore R. C., et al., 2013, ExA, 35, 413

Granot J., Piran T., Sari R., 1999, ApJ, 513, 679

Granot J., Panaitescu A., Kumar P., Woosley S. E., 2002, ApJL, 570, L61

Graziani C., Lamb D. Q., Donaghy T. Q., 2006, AIPC, 836, 117.

Hu Y.-D., et al., 2020, arXiv, arXiv:2009.04021

Huang X.-L., Liang E.-W., Liu R.-Y., Cheng J.-G., Wang X.-Y., 2020a, ApJL, 903, L26

Huang X.-L., et al., 2020b, arXiv:2012.13313

Huang Y. F., Gou L. J., Dai Z. G., Lu T., 2000, ApJ, 543, 90.

Inoue S., et al., 2013, APh, 43, 252

Ioka K., Nakamura T., 2001, ApJL, 554, L163

Ioka K., Nakamura T., 2018, PTEP, 2018, 043E02

Jacovich T., Beniamini P., van der Horst A., 2020, arXiv:2007.04418

Jordana-Mitjans N., Mundell C. G., Kobayashi S., Smith R. J., Guidorzi C., Steele I. A., Shrestha M., et al., 2020, ApJ, 892, 97

Kakuwa J., Murase K., Toma K., Inoue S., Yamazaki R., Ioka K., 2012, MNRAS, 425, 514

Lemoine M., 2015, MNRAS, 453, 3772.

MAGIC Collaboration, et al., 2019a, Nature, 575, 455

MAGIC Collaboration, et al., 2019b, Nature, 575, 459

MAGIC Collaboration, et al., 2020, arXiv:2012.07193

Murase K., Toma K., Yamazaki R., Nagataki S., Ioka K., 2010, MNRAS, 402, L54.

Murase K., Toma K., Yamazaki R., Mészáros P., 2011, ApJ, 732, 77.

Nakar E., Ando S., Sari R., 2009, ApJ, 703, 675

Nava L., Sironi L., Ghisellini G., Celotti A., Ghirlanda G., 2013, MNRAS, 433, 2107

Pe'er A., 2012, ApJL, 752, L8

Peng F., Königl A., Granot J., 2005, ApJ, 626, 966

Racusin J. L., Karpov S. V., Sokolowski M., Granot J., Wu X. F., Pal'Shin V., Covino S., et al., 2008, Natur, 455, 183

Ramirez-Ruiz E., Granot J., Kouveliotou C., Woosley S. E., Patel S. K., Mazzali P. A., 2005, ApJL, 625, L91.

Rhodes L., et al., 2020, MNRAS, 496, 3326.

Rossi E., Lazzati D., Rees M. J., 2002, MNRAS, 332, 945

Sakamoto T., Hullinger D., Sato G., Yamazaki R., Barbier L., Barthelmy S. D., Cummings J. R., et al., 2008, ApJ, 679, 570

Salafia O. S., Ghisellini G., Pescalli A., Ghirlanda G., Nappo F., 2015, MNRAS, 450, 3549

Salafia O. S., Ghisellini G., Pescalli A., Ghirlanda G., Nappo F., 2016, MNRAS, 461, 3607

Sari R., Piran T., Narayan R., 1998, ApJL, 497, L17

Sari R., Piran T., Halpern J. P., 1999, ApJL, 519, L17

Sari R., Esin A. A., 2001, ApJ, 548, 787.

Spergel D. N., et al., 2003, ApJS, 148, 175

Tomita S., Ohira Y., Yamazaki R., 2019, ApJ, 886, 54

Urata Y., Huang K., Yamazaki R., Sakamoto T., 2015, ApJ, 806, 222.

Wang X.-Y., He H.-N., Li Z., Wu X.-F., Dai Z.-G., 2010, ApJ, 712, 1232.

Wang X.-Y., Liu R.-Y., Zhang H.-M., Xi S.-Q., Zhang B., 2019, ApJ, 884, 117

Yamazaki R., Ioka K., Nakamura T., 2002, ApJL, 571, L31

Yamazaki R., Ioka K., Nakamura T., 2003, ApJ, 593, 941

Yamazaki R., Ioka K., Nakamura T., 2004a, ApJL, 606, L33.

Yamazaki R., Ioka K., Nakamura T., 2004b, ApJL, 607, L103

Yamazaki R., Sato Y., Sakamoto T., Serino M., 2020, MNRAS, 494, 5259

Yamazaki R., Yonetoku D., Nakamura T., 2003, ApJL, 594, L79

Zhang B., Mészáros P., 2001, ApJ, 559, 110

Zhang B., Mészáros P., 2002, ApJ, 571, 87

Zhang B., Dai X., Lloyd-Ronning N. M., Mészáros P., 2004, ApJL, 601, L119

Zhang B., Fan Y. Z., Dyks J., Kobayashi S., Mészáros P., Burrows D. N., Nousek J. A., et al., 2006, ApJ, 642, 354.

Zhang W., MacFadyen A., 2009, ApJ, 698, 1261

Zhang B. T.. Murase, K., et al., 2020a, arXiv:2012.07796

Zhang B. T., Murase K., Yuan C., Kimura S. S., Mészáros P., 2020b, arXiv, arXiv:2012.09143

Zhang K., et al., 2020c, arXiv, arXiv:2010.12749

Zhao W., Zhang J.-C., Zhang Q.-X., Liang J.-T., Luan X.-H., Zhou Q.-Q., Yi S.-X., et al., 2020a, ApJ, 900, 112

Zhao L., et al., 2020b, arXiv, arXiv:2012.12036